Spatially Resolved Root Water Uptake Determination Using a Precise Soil Water Sensor[1][OPEN]

Dagmar van Dusschoten,[a,2] Johannes Kochs,[a] Christian W. Kuppe,[a] Viktor A. Sydoruk,[a] Valentin Couvreur,[b] Daniel Pflugfelder,[a] and Johannes A. Postma[a,3]

[a]Forschungszentrum Jülich, Institute of Bio- and Geosciences-Plant Sciences, 52425 Jülich, Germany
[b]University of Louvain, Earth and Life Institute, 1348 Louvain-la-Neuve, Belgium

ORCID IDs: 0000-0002-6251-1231 (D.v.D.); 0000-0002-1837-759X (C.W.K.); 0000-0002-8727-3321 (V.A.S.); 0000-0002-1087-3978 (V.C.); 0000-0001-6187-2935 (D.P.); 0000-0002-5222-6648 (J.A.P.).

To answer long-standing questions about how plants use and regulate water, an affordable, noninvasive way to determine local root water uptake (RWU) is required. Here, we present a sensor, the soil water profiler (SWaP), which can determine local soil water content (θ) with a precision of 6.10^{-5} $cm^3 \cdot cm^{-3}$, an accuracy of 0.002 $cm^3 \cdot cm^{-3}$, a temporal resolution of 24 min, and a one-dimensional spatial resolution of 1 cm. The sensor comprises two copper sheets, integrated into a sleeve and connected to a coil, which form a resonant circuit. A vector network analyzer, inductively coupled to the resonant circuit, measures the resonance frequency, against which θ was calibrated. The sensors were integrated into a positioning system, which measures θ along the depth of cylindrical tubes. When combined with modulating light (4-h period) and resultant modulating plant transpiration, the SWaP enables quantification of the component of RWU distribution that varies proportionally with total plant water uptake, and distinguishes it from soil water redistribution via soil pores and roots. Additionally, as a young, growing maize (*Zea mays*) plant progressively tapped its soil environment dry, we observed clear changes in plant-driven RWU and soil water redistribution profiles. Our SWaP setup can measure the RWU and redistribution of sandy-soil water content with unprecedented precision. The SWaP is therefore a promising device offering new insights into soil–plant hydrology, with applications for functional root phenotyping in nonsaline, temperature-controlled conditions, at low cost.

Plant water use depends on multiple shoot and root traits and their interaction with environmental conditions. Aboveground, the most important environmental factors influencing plant water use are light, vapor-pressure deficit, and temperature (Vadez et al., 2014). Belowground, the spatial distribution of soil water content (θ), soil hydraulic conductivity (K[θ]), and soil osmotic potential are the most influential environmental factors for plant water uptake (Chapman et al., 2012; York et al., 2016). Plant factors determining water use include leaf area, root system length, root and shoot architecture, and the associated root, shoot and stomatal conductance (Caldeira et al., 2014; McAusland et al., 2016). Under well-watered conditions, most of the root system is redundant for water uptake. However, in drying soil, root traits such as length, distribution, diameter, age, level of suberization, expression levels of active aquaporins, xylem number and diameter, number and presence of root hairs become increasingly important for maintaining transpiration rates (Chaumont and Tyerman, 2014; Lobet et al., 2014; Lynch et al., 2014; Carminati et al., 2017; Gleason et al., 2019) as stomata will close when water supply is limited (Rodriguez-Dominguez and Brodribb, 2020). In the field, competition for limited resources makes root performance even more critical for capturing sufficient water. Studying the abovementioned traits is useful because they are under genetic control, and considerable breeding effort goes into improved survival and yield of crops under drought (Lynch et al., 2014). Complementary research focuses on water conservation management and irrigation strategies, like partial root zone drying (Sepaskhah and Ahmadi, 2012), to achieve target yields with minimal water use (Bourzac, 2013). The need for drought-tolerant cultivars and efficient water use in agriculture is outlined in several articles (Blum, 2009; Tardieu, 2012; Wasson et al., 2012). Despite many years of research, there is still considerable uncertainty as to what the important plant traits and combinations thereof are for plant water use. In part, research is hampered by lack of affordable technology for measuring spatial and temporal distribution of root water uptake (RWU), especially in relation to the

[1]This work was supported by the German Federal Ministry of Education and Research (project identification no. 031A053/DPPN to D.P. and V.A.S.), and the Belgian National Fund for Scientific Research (grant no. FC 84104No1–B086–19 to V.C.).

[2]Author for contact: d.van.dusschoten@fz-juelich.de.
[3]Senior author.
The author responsible for distribution of materials integral to the findings presented in this article in accordance with the policy described in the Instructions for Authors (www.plantphysiol.org) is: Dagmar van Dusschoten (d.van.dusschoten@fz-juelich.de).

J.K. developed the sensor; J.K., D.v.D., and D.P. built the SWaP equipment; D.v.D., J.P., and C.K. designed experiments and analyzed the data; V.S. and C.K. performed simulations; D.v.D., V.C., and J.P. developed the theory and wrote the article; all authors contributed to the text.

[OPEN]Articles can be viewed without a subscription.
www.plantphysiol.org/cgi/doi/10.1104/pp.20.00488

position and activity level of roots relative to available water (Cooper, 2016). Therefore, a low-cost sensor that is easy to build and can quantify local θ in a very precise manner would be an important technology for the study of crop response to drought and/or irrigation strategies.

Methods employed to quantify RWU are indirect, in that they measure changes of local θ or tracer concentrations over time. Because both RWU and soil water flow alter local θ or tracer concentration, reliance on modeling is considerable to dissect these components and obtain quantitative RWU numbers (Hupet et al., 2002). Currently, the most direct way to assess local RWU of parts of the root system is neutron tomography (NT) using heavy water as a tracer (Zarebanadkouki et al., 2013; Ahmed et al., 2016). RWU profiles can be reconstructed in combination with the "hydraulic architecture" theoretical framework (Meunier et al., 2017a), accounting for root conductivities varying even along each root type (Zarebanadkouki et al., 2016), as observed experimentally (Meunier et al., 2018). Fluxes in the roots can be calculated to an accuracy of ~10% (Zarebanadkouki et al., 2013). Unfortunately, NT is not very accessible, due to its price and the limited availability of the nuclear equipment needed.

Another approach relies on the measurements of isotopic ratios, e.g. ^{18}O and ^{2}H, in the xylem in relation to its sources in the soil (Zimmermann et al., 1966). Because heavy water evaporates at lower rates than normal water, the ratio of heavy to normal water varies with depth, which can then be used to quantify RWU (Rothfuss and Javaux, 2017), although with uncertain accuracy. Because this approach requires equilibrium conditions in the plant, the method is somewhat slow, and is mostly applied to a very limited numbers of plants. It does have the advantage that it can be used in the field.

The most common approach is to assess soil water content changes over time at a few different locations, i.e. typically using time domain reflectometers (TDR; Vandoorne et al., 2012). TDR is sensitive to the average soil electric permittivity around the sensor and has an accuracy to water content of ~0.01 $cm^3 \cdot cm^{-3}$ and a precision of ~0.002 to 0.003 $cm^3 \cdot cm^{-3}$ (Gong et al., 2003; Cooper, 2016). We will show here that this is insufficient for our purposes. Preferably such measurements are combined with weight change measurements of soil columns to assess plant transpiration rates (Halperin et al., 2017). Due to the superposition of redistributive soil water flow and RWU patterns, resolving these patterns based on water content time series relies heavily on inverse modeling using detailed (Koebernick et al., 2015) or more simple soil–root hydraulic models (Cai et al., 2017).

Mathematical analyses of water flow in root hydraulic architectures, analogous to conductive electrical networks (Alm et al., 1992; Doussan et al., 2006), revealed that a first component of the spatial distribution of RWU rates is solely driven by root hydraulics, architecture, and the total plant water uptake rate. We refer to it as "plant-driven RWU distribution" here normalized by soil layer volume (U_p, $cm^3 \cdot cm^{-3}\ h^{-1}$, typically called "standard" [Couvreur et al., 2012] or uncompensated RWU [Simunek and Hopmans, 2009]). It only relies on plant features and integrates over space to the total plant water uptake ($\pi r^2 \int_z U_p(z,t)dz = U_{\mathrm{tot}}(t)$, $cm^3\ h^{-1}$, which includes soil water used for transpiration and growth). A second component additive to U_p adjusts RWU distribution to total soil water potentials, which is the sum of soil matric and gravitational potentials. We refer to it as "soil-driven root water uptake redistribution," also normalized by soil layer volume, U_s, $cm^3 \cdot cm^{-3}\ h^{-1}$, typically called "compensatory" (Couvreur et al., 2012) or "compensation" RWU (Jarvis, 1989). It relies on soil water potential heterogeneity and spatially integrates to zero as per definition. Note that here U_s, U_p, and U_{tot} are defined negative when removing water from the soil. Only in limited cases (locally $-U_s < U_p$) is hydraulic lift observed (Caldwell and Richards, 1989). The impact of these simultaneous processes on the observed θ-profile can be modeled employing an extended one-dimensional (1D) Richards equation following Couvreur et al. (2014a, 2014b):

$$\frac{\partial\theta(z,t)}{\partial t} = U_p(z,t) + U_s(z,t) + \frac{\partial}{\partial z}\left[K(\theta(z,t)) \times \left(\frac{\partial h(z,t)}{\partial z} - 1\right)\right] + \begin{cases} E_s(t), z = 0 \\ 0, z \neq 0 \end{cases} \quad (1A)$$

where K ($cm\ h^{-1}$) is the soil unsaturated hydraulic conductivity, h (cm) is the soil matric potential, and E_s ($cm^3 \cdot cm^{-3}\ h^{-1}$) is the soil surface water evaporation rate per unit soil layer volume ($\pi r^2 \cdot \Delta z$, with r as the inner pot radius in centimeters).

Many of the parameters and variables in Equation 1A are difficult to determine. Specifically, soil hydraulic conductivity is difficult to measure and is often derived theoretically with considerable uncertainty (Baroni et al., 2010). Root architecture and hydraulic conductivity data, which could be used to estimate U_p and U_s terms, are also hardly accessible experimentally, although some are available in the literature (Doussan et al., 2006; Ahmed et al., 2018). Yet, root conductivity may change with environmental conditions and can have a circadian rhythm (Sakurai-Ishikawa et al., 2011; Caldeira et al., 2014; Chaumont and Tyerman, 2014).

From a simpler perspective, the divergence of soil water capillary flow rates and U_s are both driven by—and tend to reduce—soil water potential heterogeneity, while being instantaneously independent of U_{tot}. Therefore, we gather them under the term "soil water redistribution," S_r (s^{-1}, equal to $U_s(z) + \frac{\partial}{\partial z}\left(K(\theta(z,t))\left(\frac{\partial h(z,t)}{\partial z} - 1\right)\right)$), in the following version of Equation 1A:

$$\frac{\partial\theta(z,t)}{\partial t} = \hat{U}_p(z) \cdot \frac{U_{\mathrm{tot}}(t)}{V} + S_r(z,t) + \begin{cases} E_s(t), z = 0 \\ 0, z \neq 0 \end{cases}, \quad (1B)$$

where V equals total soil volume, the normalized variable $\hat{U}_p(z) = \frac{U_p(z)}{U_{\mathrm{tot}}} \cdot V$ (positive, and $\int_z \hat{U}_p(z)dz = 1$).

Furthermore, S_r values are null when the total soil water potential is spatially uniform, and by definition $\int_z S_r(z,t)dz = 0$. The relevant processes are schematically presented in Supplemental Figure S1.

In this study, we present a sensor of soil water content, the soil water profiler (SWaP), and propose a method to estimate the vertical distribution of the plant-driven RWU distribution as demonstrated for maize (*Zea mays*). Assuming that on an hourly timescale, $\hat{U}_p(z)$does not vary, e.g. no substantial growth and S_r evolves linearly with small variations of h (soil matric potential only), then relatively fast light-induced modulations of U_{tot} generate variations of the profile of $d\theta(z)/dt$ directly proportional to $\hat{U}_p(z)$. Measuring such small variations of $d\theta(z)/dt$ requires unprecedented precision, which can only be reached with the new SWaP device presented in this article. The idea of using day–night fluctuations of transpiration to separate RWU from soil water flow using synthetic data has been previously proposed (Guderle and Hildebrandt, 2015). However, our approach is to perform it on considerably shorter timescales with experimental laboratory data.

RESULTS

Sensor Characteristics

We constructed a sleeve-like sensor with two opposing copper sheets (internal diameter of 9 cm, sheet area of 5×7 cm^2) that function as a capacitor (Fig. 1A) with a pot (9-cm diameter, 50-cm length) standing free within the sensor. When the sleeve with copper plates is connected to a coil this yields a resonant circuit whose resonance frequency (f) depends on the capacitance (C) as follows: $f \sim 1/\sqrt{C}$. This circuit is coupled inductively, via a second, identical coil with 2-mm spacing, to a vector network analyzer (VNA) working in input reflection mode (S_{11}) to determine the resonance frequency (an example is shown in Fig. 1B). The resonance frequency depends on the average permittivity between the copper plates (see "Materials and Methods") and can therefore be used to determine $\theta(z)$ using a calibration curve (Fig. 1D). The system has been multiplexed to four sensors using a PIN diode switch, with all four sensors being shifted longitudinally by a stepper motor along a linear axis. This construction forms our SWaP.

The four independent sensors have an average resonance frequency of 250.4 MHz (SD = 1.4 MHz) when unloaded, which drops to 156.9 ± 1.3 MHz when our soil is water-saturated ($\theta = 0.32$). The deviations of the resonance frequencies under climate chamber conditions equaled 3 kHz. The relative electric field (E-field) vertical distributions of each of the sensors are displayed in Figure 1C, expressed in frequency shifts relative to the unloaded resonance frequency (f_0; Sydoruk et al., 2016). Each data point represents four individual resonance frequency measurements. Additionally, the simulated E-field distribution of a sensor as calculated on the platform Comsol (https://www.comsol.com/) is added to Figure 1C (see "Materials and Methods"). The simulated and measured E-field distributions agree to a very large extent that gives confidence that the simulation model can also be used to predict other features of our setup. Whereas the total E-field depth (in z-direction) covers 12 cm, 95% of the summed field strength, corresponding to its sensitivity, occurs with the inner 8 cm. The simulated horizontal field distribution is presented in Supplemental Figure S2.

Because the electric permittivity is also temperature-dependent and the climate-chamber lamps cause small variations in temperature, the influence of temperature on the resonance frequency was determined. Across the temperature range of 16°C to 24°C, we recorded a 12 ± 4 kHz $°C^{-1}$ temperature-drift coefficient. Furthermore, we verified the dependency of the resonance frequency on different nutrition solution strengths, tested up to 7 mS cm^{-1}, but observed no influence on the resonance frequency in the tested range.

The sensitivity of each of the sensors to known soil water content, determined gravimetrically, was determined in stationary mode that yielded the calibration curves, plotted in Figure 1D. The calibration curves could be fitted with a second-order polynomial with an average 95% confidence interval (CI) of 0.003 $cm^3 \cdot cm^{-3}$ and an average initial slope of 2.67 MHz $cm^3 \cdot cm^{-3}$. We excluded from the calibration those samples that were very wet (θ between 0.16 and 0.32), as in our sandy soils such wet samples were very sensitive to handling. These wet samples compacted easily and built up nonlinear soil water content gradients quickly. At full saturation, measured with a closed base, no soil water content gradients occur, so this point could also be measured reliably.

In addition to the calibration at known soil water contents, the sensor's response to soil-filled tubes was simulated using a physical model of the sensor using the platform Comsol. The results of these simulations are also presented in Figure 1D (solid line), showing good agreement with the measured data with a root mean square error of 0.68 MHz.

Scanning Mode Validation

Given the good results for homogeneous samples, we tested the SWaP in scanning mode on nonhomogeneous samples. Such scans were performed automatically to measure θ-profiles for four 45-cm soil columns with and without maize plants every 24 min. Two steps were required before profiles of θ or $d\theta/dt$ could be determined: deconvolution over space, and conversion of resonance frequency data to θ. Deconvolution is a procedure that corrects for the fact that our sensor is sensitive over a length (z') of 12 cm instead of the desired resolution of 1 cm. Each 1-cm layer contributes to the capacitance weighted with the relative electrical field strength at that position. This contribution can be

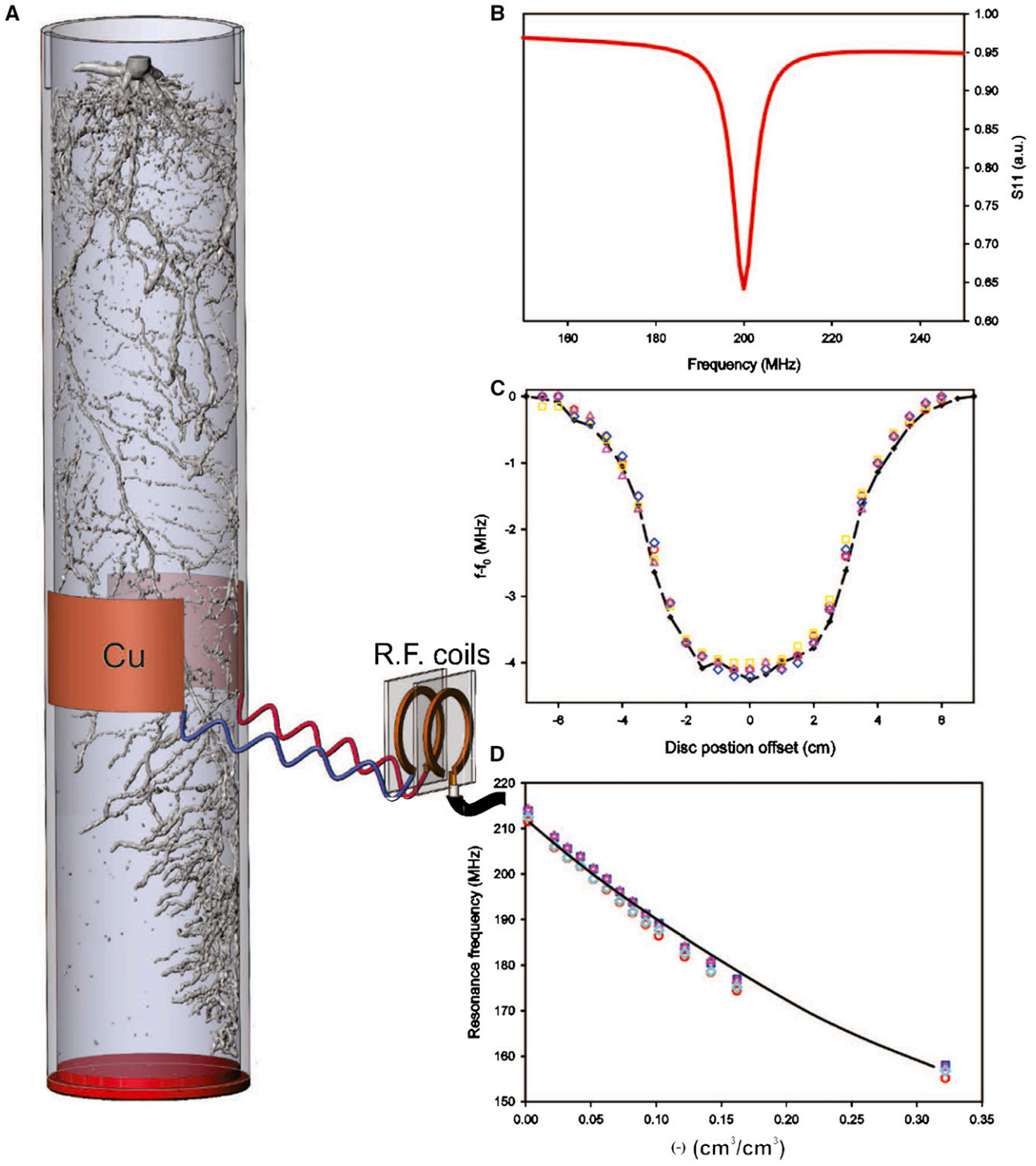

Figure 1. Schematic drawing of the SWaP, the raw data it generates, and relevant curves to calculate soil water content (θ) profiles. A, Drawing of the SWaP without casing, showing the copper sheets (brown areas, one marked with Cu) that function as capacitor. B, The two radio frequency (R.F.) coils inductively coupling the sensor to a VNA that generates input reflection (S_{11}) data. a.u., Arbitrary units. C, The relative E-field distribution, expressed in frequency shifts relative to the unloaded resonance frequency (f_0), $E(z')$ of each sensor (represented by different symbols) and the simulated E-field using the platform Comsol (black line). D, Calibration curves of the soil water content (θ) against the resonance frequencies for all sensors (represented by different symbols). Black line represents the predicted sensor response (see "Materials and Methods").

retrieved by measuring at several z-positions and undoing the sensors' convolution or blending using a deconvolution procedure. The deconvolution and calibration procedures are described in more detail in "Materials and Methods."

First, we demonstrate how the model-constrained deconvolution method performs under realistic circumstances, including the presence of a plant. In Figure 2A, a typical resonance frequency profile (solid circles), the fitted model of the data before deconvolution ($f(z)$, solid red line) $r^2 > 0.99$, and the deconvoluted model ($g(z)$, dashed blue line) are presented for a soil column close to water holding capacity. As expected, the deconvoluted model deviates significantly from the raw data at the edges, because the permittivity outside the soil columns has very different values and is blended with those inside the soil column owing to the sensor's sensitivity profile. Because of the very low noise of our sensor, an equidistant three-point time derivative of the scanning data can be made for each z-position. Figure 2B presents the change of the resonance frequency profile with time for 45 z-positions for two different cases: one with a transpiring maize plant during daytime (solid circles), and one with a maize plant at night (gray squares). Here too, the modeled, convoluted polynomials, $df(z)/dt$ (solid red line) and $r^2 > 0.99$ (magenta line), follow the data quite well. The deconvoluted model, $dg(z)/dt$, is presented by dashed blue or cyan lines. Both $g(z)$ and $dg(z)/dt$ can be converted to $\theta(z)$ and $d\theta(z)/dt$, respectively, using the calibration curve.

Second, we compared $\theta(z)$ obtained using the SWaP with two types of measurements.

Type I: After a SWaP scan, small quantities of soil were excavated (10 to 20 cm^3) at known positions, for which the local water content was determined gravimetrically. These values were compared to $\theta(z)$ measurements with the SWaP in scan mode. The results and fit ($y = 0.0013 + 0.997x$) are plotted in Figure 2C with the 95% CI as dashed lines. At the bottom of the soil

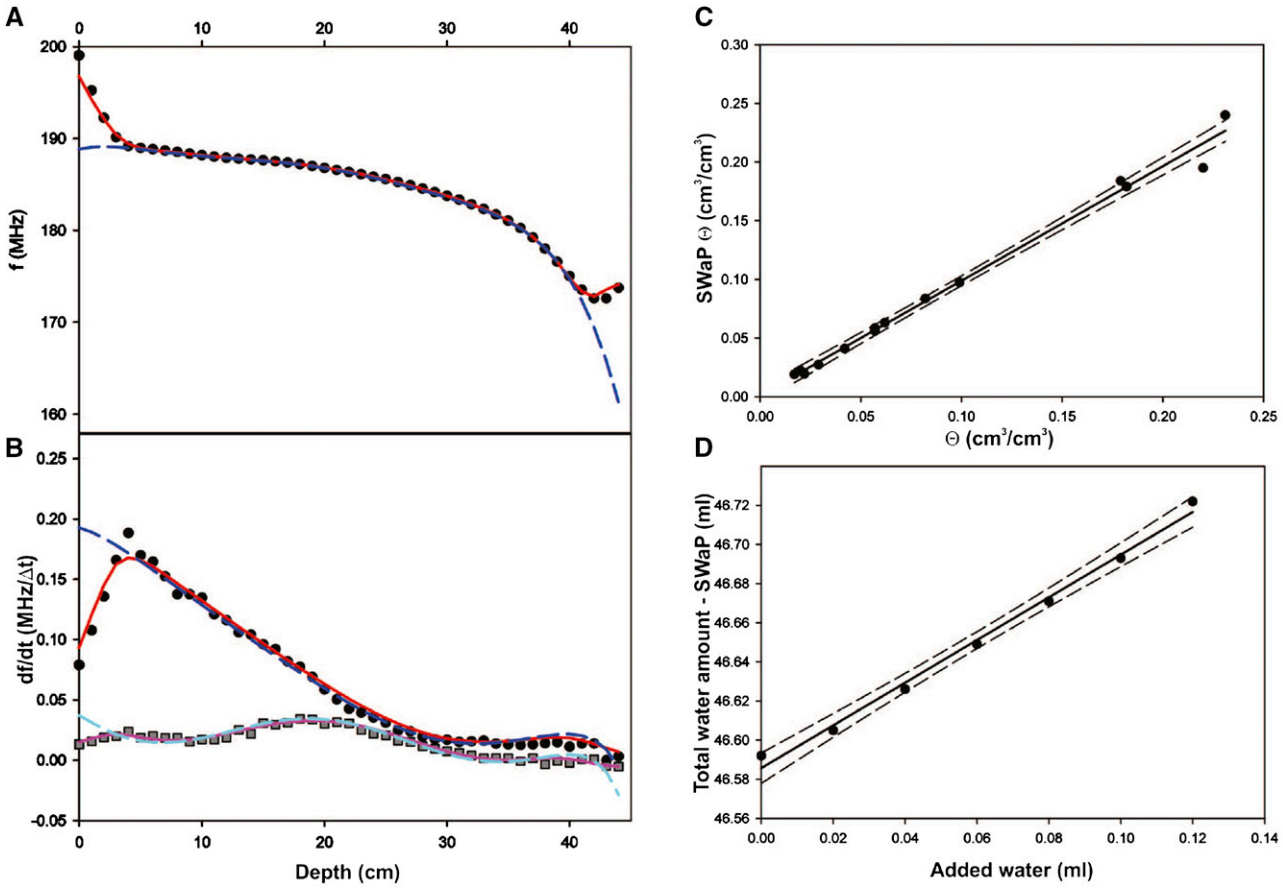

Figure 2. Typical frequency profiles along soil-filled columns, the time derivatives thereof, and some validation data. A, Profile of resonance frequency, $f(z)$ (black dots); the fit results (red lines); and the deconvoluted frequency profile $g(z)$ (dashed blue line). B, Profile of time derivative of the frequency profile, $df(z)/dt$ for soil column with maize plant during daytime, $df(z)/dt$ (black dots), fit results (red line), and $dg(z)/dt$, the deconvoluted time derivative (dashed blue line); and during night-time, $df(z)/dt$ (black squares), fit results (magenta line), and $dg(z)/dt$ (dashed cyan line). C, Gravimetrically determined soil water content (θ versus θ) obtained with SWaP and the fit ($y = 0.0013 + 0.997x$) with the 95% CI (dashed lines). D, Change of soil column water amount versus sequential additions of 20 μL of water including fit (black line) and the CI (dashed lines).

column, where θ is largest, we observe a reduced accuracy of ~0.005 $cm^3 \cdot cm^{-3}$—probably due to deviations of the E-field distribution close to sharp edges. Moreover, at the edges, both at the top and the bottom, noise is enhanced because these slices were measured less frequently.

Type II: We added known amounts of water to the soil columns and monitored the change of the integrated amount of water as determined by the SWaP. The smallest amount of repeatedly added water we could detect was 20 μL for our 2.4-L soil columns. These results are presented in Figure 2D. We found a slope of 1.1 ($r^2 = 0.993$; $CI = 8$ μL).

Quantification of Plant Water Uptake and Redistribution in Soil Columns

Soil water depletion measurements in cylindrical pots with growing maize seedlings started after the shoot emerged from the soil, 4 d after sowing (DAS). At the three-leaf stage (11 DAS), oscillations of the soil water depletion rate caused by the light-induced, modulating transpiration rate of the maize plant were sufficiently large to distinguish them from temperature-related oscillations on a local (z) level, but insufficient to perform a reliable analysis. After a few more days, an increasing shoot size caused increased soil water-depletion rates and more pronounced modulations thereof, which is exemplified in Figure 3. Figure 3A depicts two soil water-content curves measured over a 3-d period at a relatively low depth ($z = 8$ cm) relative to the surface. The combined noise and temperature drift of these curves was as low as 6×10^{-5} $cm^3 \cdot cm^{-3}$. The blue data points were acquired starting at nine DAS and the black data points at 15 DAS. The time derivatives of these traces, the soil water-depletion rates, are plotted in Figure 3B. Additionally, the sum of the soil water depletion rates of the whole column ($\sum_z \frac{\partial\theta(z,t)}{\partial t} = \frac{U_{tot}(t)}{A\sum_z \triangle_z} + E_s(t)$) starting at 15 DAS is plotted (red line), scaled down by a factor of 10 for visual comparison. Soil water depletion was clearly faster during daytime (orange blocks at the bottom of Fig. 3B). Within each day, three oscillations of U_{tot} synchronous with high- and low-light levels in the chamber are visible (range annotated by arrow labeled "M"; low daytime U_{tot} annotated by arrow labeled "NM"). We also note that during the night, while the column is still losing water (red line), the zone at z = 8 cm shows some positive values for $d\theta/dt$ at night, indicative of a form of redistributive water flow.

Disentangling the U_p component of RWU from soil water redistribution (S_r; see Eq. 1B) required the estimation of U_{tot} and E_s, as well as the simplifying assumption that within a 12-h window, S_r is well described by a linear regression: $S_r(z,t) = p_1(z) + p_2(z) \cdot t$. This is the simplest model for S_r that is physically sensible, as we know that RWU induces changes of $h(z)$, driving variations of soil water redistribution over time (see further below for supportive data). The fact that U_{tot}, S_r, and $\hat{U}_p$ vary on different timescales (see further below) allowed the use of clearly distinct functions to fit the $d\theta/dt$ data.

Based on Equation 1B and the simplifying assumption of S_r, the local soil water depletion rate at any given position (z) within a 12-h window was thus modeled as

$$(2)\quad \partial\theta(z,t)/\partial t = \hat{U}_p(z) \cdot \frac{U_{tot}(t)}{V} + p_1(z) + p_2(z) \cdot t + \begin{cases} E_s(t), z = 0 \\ 0, z \neq 0 \end{cases}, \qquad (2)$$

Evaporation was determined independently by monitoring soil water depletion in a column without a plant, and subtracted from evapotranspiration, which is estimated as the spatial integral of the soil water depletion rates, to yield U_{tot}. The remaining unknowns $\hat{U}_p(z)$, $p_1(z)$, and $p_2(z)$ were fitted by least-square regression of $d\theta/dt$, e.g. dashed blue lines and black data points in Figure 3, C and D, respectively, for each z-position independently. The modulation amplitude of $d\theta/dt$ relative to M in Figure 3B is sufficient to determine $\hat{U}_p$. $U_p(z,t)$ was then calculated by multiplying $\hat{U}_p(z)$ and $U_{tot}(t)$. Even though the parameterization was completed independently for each depth, the vertical integrals of $\hat{U}_p(z)$ and of $p_1(z) + p_2(z) \cdot t$ always converged to 1 and 0 with accuracies of 10^{-5} and 10^{-7}, respectively.

In Figure 3, C and D, soil water depletion rate data at two depths is presented for two different maize plants with different rooting depths, as evidenced by magnetic resonance imaging (MRI) data, with $t = 0$ h when the lights are switched on. Figure 3C depicts $d\theta/dt$ data collected from a well-watered, shallow-rooted maize plant in a well-rooted zone ($z = 8$ cm, black circles) and a nonrooted zone ($z = 21$ cm, gray squares) a few centimeters below the deepest root. High light periods are denoted by yellow blocks at the bottom of Figure 3D. The plant-driven component of RWU normalized by the soil layer volume was isolated based on Equation 2 (red line; $z = 8$ cm, dashed magenta; $z = 21$ cm). Its summation with S_r adequately fits the measured $d\theta(t)/dt$ data at $z = 8$ cm, represented by the blue dashed line, $r^2 = 0.95$. In the nonrooted zone (Fig. 3C, $z = 21$ cm) we find no evidence of RWU (see magenta dot-dashed line for U_p), but we do observe soil water depletion owing to vertical soil capillary flow. Here, squares and cyan line present measured and modeled $d\theta(z,t)/dt$, respectively, which follows our simple model $S_r(t) = p_1 + p_2 \cdot t$. The same type of data and its model results are presented in Figure 3D for a well-watered, deeper-rooted plant, but with a higher root length density (RLD) at $z = 8$ cm (black circles) than at $z = 21$ cm (gray squares, $r^2 = 0.95$).

Plant-driven water uptake distribution and soil water redistribution were calculated as described above for each layer. The corresponding profiles are plotted in

Figure 4, A and B. Additionally, the RLD distribution ($RLD[z]$) obtained from MRI root images and subsequent analysis with NMRooting (van Dusschoten et al., 2016) is presented using black squares, and inverted for easy visual comparison. U_p (t = 8 h) is represented by the solid red lines for a shallow-rooted maize plant in Figure 4A and a deep-rooted maize plant in Figure 4B. A strong correlation between plant-driven RWU and the RLD distribution was observed for all four maize plants whenever the soil column was close to its water-holding capacity, as it was watered the day before and had a rather uniform soil water matric potential. See, as an example, the lower line in Supplemental Figure S4; the maximum difference between the bottom and top of the soil column is −3 kPa in matric potential. The Pearson correlation coefficient between $RLD(z)$ and $U_p(z)$ ranged between 0.89 and 0.95, for four plants at seven different instances, with a minimum modulation in uptake rate amplitude of 0.3 $cm^3\ h^{-1}$. The dotted magenta line represents the soil water depletion rate (t = 8 h), and only roughly follows $RLD(z)$, with a Pearson correlation coefficient of 0.6. Note that, at the bottom, the soil water depletion rate (t = 8 h) turns positive, owing to earlier watering from the top and subsequent, downward movement of this water.

Our analysis also yields soil water redistribution profiles that we assume are linearly dependent on time within each 12-h window, as a first-order approximation. To validate this assumption, we compared the measured soil water depletion rates at night (represented by red and blue dots in Fig. 4C) for deep- and shallow-rooted plants, respectively. Here, plant water uptake is minimal, so that we approximatively measured $S_r(z)$, with extrapolated $S_r(z)$ based on our model (see red and blue curves in Fig. 4C). The measured and model-based, extrapolated $S_r(z)$ agreed reasonably well ($r^2 > 0.9$ for both plants). This suggests that our linear model for S_r is a reasonable assumption.

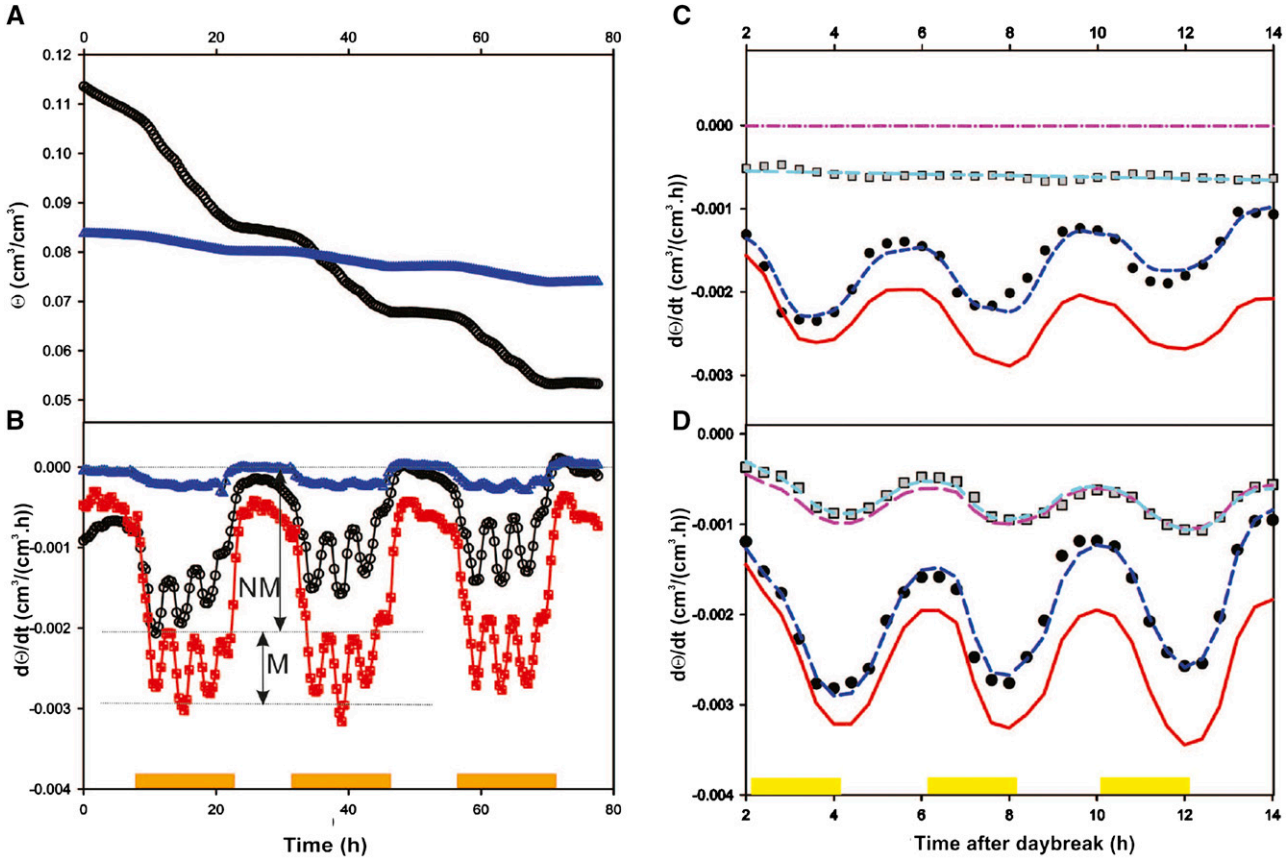

Figure 3. Soil water depletion curves of soil columns with maize plants. A, Three-day period time series of soil water content, $\theta(z = 8\ cm)$ with a transpiring maize plant starting at 9 DAS (blue data points) and 15 DAS (black data points). B, Same data but now soil water depletion rate $d\theta(z = 8\ cm)/dt$. Added is a $U_{tot}+E_s$ curve (evapotranspiration rate), scaled down for visual comparison (red squares). Orange squares at the bottom denote daytime. The relative amplitude of the U_{tot} modulation is indicated by the lengths of the arrows labeled "M" and "NM" (nonmodulated transpiration). C, Time series of soil water depletion rate, $d\theta/dt$ for shallow-rooted maize plant over 12-h period after lights were switched on (15 DAS). Yellow blocks at the bottom indicate high light. Black dots are $d\theta(z)/dt$; red line is plant-driven RWU, $U_p(z = 8\ cm)$; dashed blue line includes soil water redistribution. Gray squares are $d\theta(z)/dt$, magenta dash dots are $U_p(z = 21\ cm)$, dashed cyan line includes soil water redistribution. D, Time series of a deeper-rooted maize plant. See C for explanation.

For the above analysis, we assume that $\hat{U}_p(z)$ is time-invariant during the 12-h experimental time window. This can be verified by reducing the time window for the analysis to 4 h and performing the analysis for three subsequent time periods on 1 d. We performed this check for 12 different whole-day measurement series (three plants on four different days each) and found low SDs among the three 4-h time-periods $\hat{U}_p(z)$ values for each plant during the 12-h periods (average SD $<$ 0.0075). This confirmed that in these experiments $\hat{U}_p(z)$ was sufficiently stable during the day (Supplemental Fig. S3).

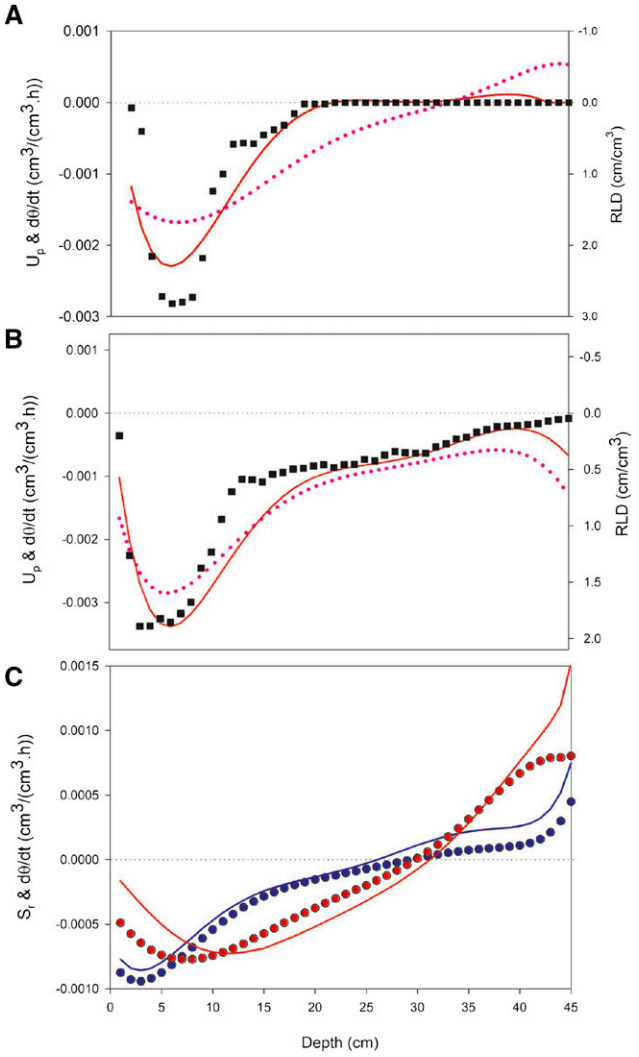

Figure 4. Depth profiles of $U_p(z)$, $RLD(z)$, $S_r(z)$, and $d\theta(z)/dt$. A, Plant-driven RWU, $U_p(z)$ of a shallow-rooted maize plant (red line) and the inverted RLD profile, $RLD(z)$ (black squares), and $d\theta/dt$ at noon (15 DAS, magenta dots). B, Same data as A for a deeper-rooted maize plant. C, Soil water depletion rate, $d\theta/dt$ shortly before lights were switched on for two maize plants at 15 DAS (red circles, shallow-rooted maize plant; blue circles, deep-rooted maize plant) and the predicted soil water redistribution S_r (red line, shallow-rooted maize plant; blue line, deep-rooted maize plant) for both plants.

Proof of Concept of $\hat{U}_p(z)$ Retrieval Using In Silico Observations

To verify if known plant-driven RWU rates could be accurately estimated from the soil water depletion rate under modulating plant transpiration rate, we used numerical simulation of soil–plant hydrodynamics to generate in silico observations of soil water depletion rate profiles, and then applied Equation 2 to retrieve $\hat{U}_p(z)$. The results of these in silico experiments are presented in Supplemental Figure S5 with a more extensive description. The main findings are that $\hat{U}_p(z)$ is retrieved most reliably when the modulation period is short, at maximum six hours, otherwise $\hat{U}_p(z)$ is smeared out over 5 cm or more. Also, $\hat{U}_p(z)$ is retrieved more reliably when soil conductivity is lower in the sense that less smearing occurs.

From the comparison between our imposed and retrieved $\hat{U}_p$ profiles, we conclude that the proposed approach of soil water depletion rate profile monitoring under modulating transpiration rate is a reliable method to separate profiles of plant-driven RWU from soil water redistribution, given the sufficient sensitivity of the SWaP device.

RWU in Drying Soils

In conditions close to soil water-holding capacity, the investigated maize plants showed a higher RWU rate near the soil surface (Fig. 4B), closely related to the higher RLD there. In consequence, water depletion was more pronounced in the upper half of the profile, generating substantial vertical gradients in θ and soil water potential over timescales of several days. Under such conditions, we observed increasing rates of soil water content change lower in the profile. Disentangling $U_p(z)$ from $S_r(z)$ with Equation 2 allowed us to interpret that this trend was caused by a net downward trend of $U_p(z)$ on four consecutive days, as depicted in Figure 5A. Here data are presented always 4 h after the light was switched on. On the fourth day (26 DAS) after watering, the maize plant reduced its transpiration rate considerably after 4:00 PM, so these data were excluded from the analysis as presented here. The soil water matric potential data for these measurement days is given in Supplemental Figure S4. The difference in soil water potential between the top and the bottom consecutively reached 3, 15, 80, and 430 kPa during these 4 d. Figure 5B depicts a comparison between two instances, one with high, the other with lower light, for $U_p(z)$, red and blue lines respectively, and the concurrent soil water depletion rates, the red and blue circles, on 25 DAS, which is 3 d after watering. The differences between $U_p(z)$ and the soil water depletion rates are caused by soil water redistribution (S_r), which is nearly identical for both instances (reduction of $<5.10^{-5}$ cm^3 · cm^3 h^{-1} during 2 h). The data shows clearly that at high light, the soil water depletion rate

profile better approximates $U_p(z)$ than at lower light, where the depletion rate has a completely different profile and is nearly flat.

In Figure 5C, the ratio of $U_p(z)$ to $RLD(z)$ is used to color an MRI image of a root system, which approximates the RWU per unit length of root when redistributive water uptake (U_s) is minimal because of the small soil matric potential difference (3 kPa) at this time. Figure 5D presents the same ratio under a vertical difference of 430 kPa, with θ ranging from 0.07 to 0.025 $cm^3 \cdot cm^{-3}$ from bottom to top of the column. To determine the correct soil water content numbers, MRI data were used to correct for the root mass, which is also detected by the SWaP and cannot be distinguished from soil water. Especially when the soil is dry this correction is important because the amount of water in the roots (~1% volume at the top) is comparable to the soil water content, being in the range of 2.5%. Ignoring this contribution leads to a considerable underestimation of $h(z)$. This error is typical for sensors that depend on the electrical permittivity to determine soil water content, like TDR. The changes of the root lengths over the 4-d period are clearly not mimicked by the ratio of $U_p(z)$ to $RLD(z)$, which suggests that root hydraulic properties may have been altered between the wet and dry conditions.

DISCUSSION

Our results show that we successfully developed an accurate (0.002 $cm^3 \cdot cm^{-3}$) and especially highly precise (6.10^{-5} $cm^3 \cdot cm^{-3}$) soil water content sensor adapted to soil columns in climate chambers, more than

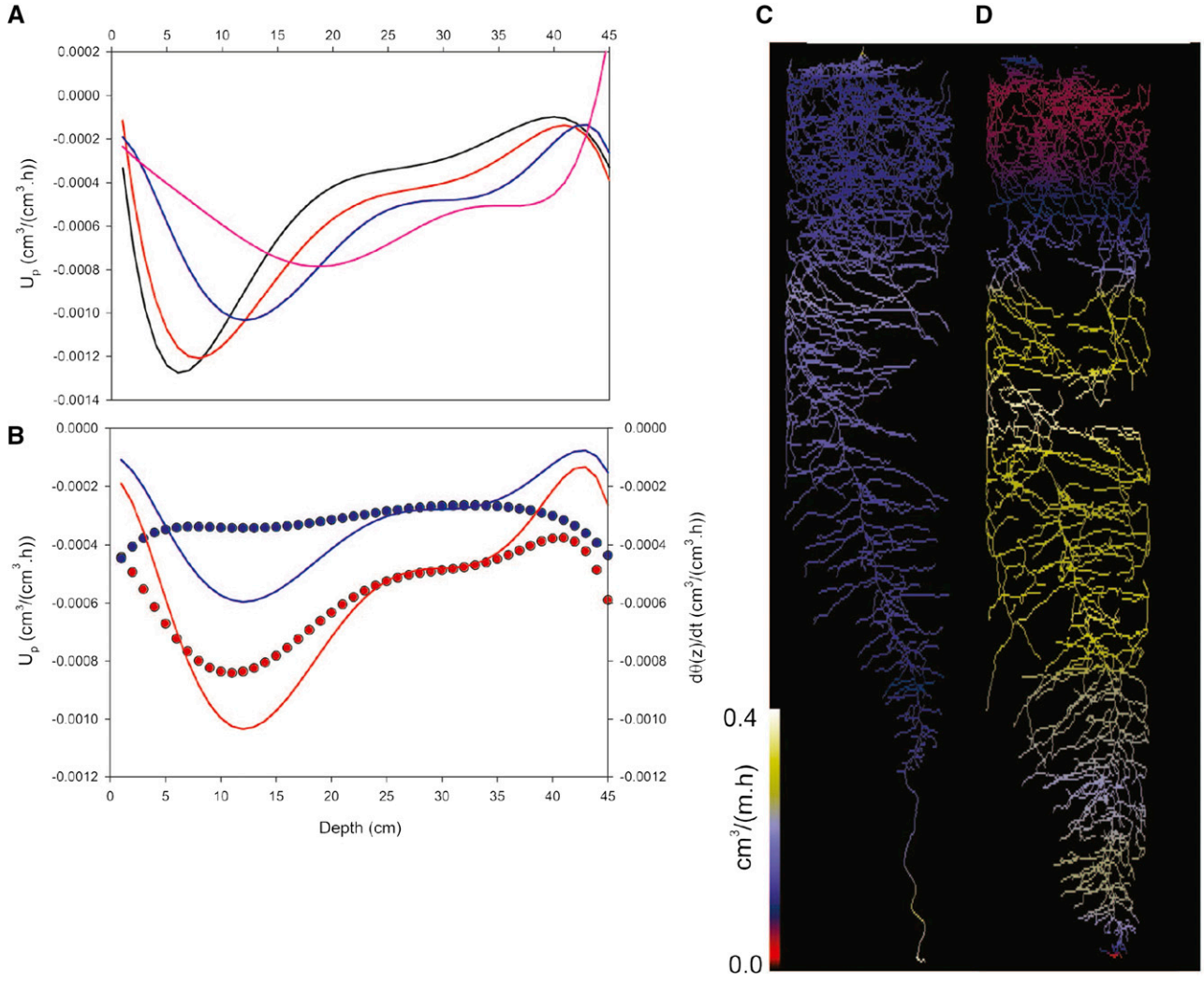

Figure 5. Effect of progressive drying of soil on the plant-driven water uptake distribution. A, Plant-driven RWU, $U_p(z)$ on four consecutive days (23, 24, 25, and 26 DAS; black, red, blue, and magenta lines, respectively). B, Effect of light intensity on the soil water depletion rate, $d\theta/dt$ (circles) in comparison to $U_p(z)$ (lines) on 25 DAS. High light, red circles and lines; low light, blue circles and lines. C, Root maps of a maize plant at 21 and 27 DAS color-coded by normalized plant-driven RWU (divided by RLD × column V), $U_p(z)/RLD(z) \cdot V$. D, Same type of data as in C, now on 26 DAS.

an order-of-magnitude more precise than commonly available tools like TDR and frequency domain reflectometry (Cooper, 2016). Furthermore, the sensor's 1D spatial resolution theoretically reaches 1 cm, and its continuous nature also allows spatial integration of $\theta(z)$ to track a soil column's total water content dynamically for multiple columns simultaneously. We determined local soil water content depletion rates and their variations as induced by transpiring maize plants. At an hourly timescale, modulating transpiration with varying light intensities allowed decoupling of the plant-driven RWU from the soil water redistribution signals quantitatively.

The SWaP Sensor Specificity

Because resonance frequencies can be determined very accurately, we build the soil water-content sensor as a resonant circuit. Also, we placed the copper plates that form a capacitor outside of our medium such that a more homogeneous E-field is generated, especially in the horizontal plane. Compared to TDR or frequency domain reflectometry sensors (Bore et al., 2016), this gave a better weighing of the different regions within or around the sensor (see Supplemental Fig. S2). As we demonstrated in the results, our design with inductive coupling and shielding results in a sensor with a very high, usable dynamic range factor of 20,000.

The gain in accuracy is also very good although not as high, because water distribution in larger volumes is not a priori known relative to the E-field distribution. Therefore, calibration was not possible between 16% and 32% because of rapid downward water mobility, causing a gradient in water distribution, and thereby soil compaction, which may be a limiting factor for accuracy. During scanning, at the edges of the soil column, the E-field distribution is distorted and errors in the range of 0.5% to 1.0% may be expected, and in our validation we never found deviations $> 1\%$ (see Fig. 2). This means that scanning does not introduce additional errors except for close to the soil column edges. We obtained confirmation for the quality of the scanning data when we added water volumes, down to 20 μL, at the top of the soil column and were able to detect the change with sufficient accuracy (see Fig. 2D). This experiment was performed under laboratory conditions, otherwise temperature fluctuations would have masked the small frequency changes caused by adding such small amounts of water to a large column. Temperature sensitivity of the sensor can pose a problem when temperature is not precisely controlled. Despite the above limitations, the overall performance of the SWaP offers a considerable improvement in soil water content profiling, especially in regard to the simplicity and cost of the equipment. This ability to determine soil water content profiles by itself is very useful and important, as it provides a rapid method to determine the soil water content profile in relation to plant performance, like growth and transpiration related to soil water distribution.

The variations in $d\theta(z)/dt$ were detectable at a very early stage when the leaf area was ~20 to 30 cm^2. At 8 cm below the surface we initially only observed the indirect effect of surface evaporation on soil water depletion, which is slightly higher with light than without (Fig. 3, A and B). In an earlier implementation of the SWaP where the resonance frequency was simply approximated by the frequency showing minimal reflection, noise levels limited our precision to 0.1% to 0.2% $cm^3 \cdot cm^{-3}$, comparable to high-end TDRs (Gong et al., 2003). These noise levels were still ~10 times too high to detect the light-induced variations in $d\theta(z)/dt$ (e.g. compare with Fig. 3B). Even for plants with a leaf area of 400 cm^2, which deplete soil water in a few days, noise levels of 0.1% $cm^3 \cdot cm^{-3}$ are not low enough to observe varying uptake rates, with typical modulation amplitudes of $d\theta/dt$ of <0.002 $cm^3 \cdot cm^{-3}$ h^{-1}, when light levels change between 400 and 700 $\mu E \cdot m^2 s^{-1}$. It requires very high precision θ-measurements to be able to observe the effects that we described here, which explains why it is not described elsewhere. Once the plants were sufficiently large, the modulation patterns in the soil became usable for further analysis.

The temporo-spatial water content profiles that our sensor collects may also be compared to those obtained with NT. NT offers higher dimensionality (mostly 2D) and spatial resolution, but is a very expensive technique not generally available to plant biologists or hydrologists. The very precise soil water sensors that we showed here are rather easy to build, and come at low cost; our current prototype with four sensors cost ~1,500 € to build, is portable (can be used in climate chambers) and is completely harmless to the plant. A combination with a fully programmable water-cooled LED panel should be profitable as it minimizes thermal influences and should help with resolving light-dependent and light-independent RWU rates. This then constitutes a new, versatile tool to probe RWU profiles in relation to water management strategies and genotype-specific responses.

From Water Depletion Rate to Uptake and Redistribution Profiles

We presented a simple model to quantify the fraction of local RWU that varies proportionally to the plant transpiration rate, or plant-driven RWU distribution by layer-wise fitting soil water depletion rate data to Equation 2 using total water uptake U_{tot} as independent parameter. Measured $U_p(z)$ should closely approximate RWU when the profile of soil water potentials is uniform (Couvreur et al., 2012). When it is not, the only difference between $U_p(z)$ and $d\theta(z)/dt$ is the soil water redistribution $S_r(z$; through soil and roots). This profile can be estimated with a methodology also described by Guderle and Hildebrandt (2015), provided that S_r variations remain nonmodulating (owing to soil water capacitance) during the light modulations.

By observing layers just below the lowest roots, information that we can glean from MRI data, we could

verify experimentally that S_r does not fluctuate there and also changes approximately linearly with time. An example of the absence of modulations in the soil water depletion rate is given in Figure 3C, but can be seen to persist farther away from the roots as well (see Fig. 4A). Additionally, our forward simulation studies (see Supplemental Fig. S5) confirm that the effect of the plant-driven RWU modulations on the soil water depletion rate dampens out in the soil within a few centimeters when these modulations occur within 6 h, even when the simulated $U_p(z)$ has a sharp front. These simulations therefore suggest this does not work well on a day–night timescale. The combination of these findings indicates that under the conditions we are working with, $S_r(z,t)$ should not show considerable modulations.

In drying soil with a considerable vertical water potential gradient (25 DAS), modulating transpiration rate using moderate and higher light intensity levels (400 and 700 μmol m^2 s^{-1}, respectively) was key to show the independence between soil water redistribution $S_r(z)$ and $U_p(z)$ profiles, as demonstrated theoretically by Couvreur et al. (2012). In contrast, Figure 5B shows that their shapes differ significantly (see blue and red circles $d\theta(z)/dt$ under moderate and high light, respectively). Hence, in drying conditions $RWU(z)$ is a mix of independent shoot- and soil-driven water flow dynamics, U_p and U_s, respectively. It also demonstrates the importance of light intensity when studying plant drought stress, as water-depletion zones will develop quite differently under high as compared to low transpiration rates.

The Plant-Driven Water Uptake Distribution as a Proxy for RLD

Our results in soil close to its water-holding capacity support experimentally the common assumption that overall U_p and RLD profiles scale proportionally ($r^2 = 0.95$; Feddes et al., 2001; Lobet et al., 2014; Albasha et al., 2015), here for young maize plants. The original underlying hypotheses are that root axial conductivity is high while root radial conductivity is relatively uniform across roots (Steudle and Peterson, 1998), even though some studies suggest this need not hold always (Ahmed et al., 2018). Alternatively, a limiting axial root conductivity combined with a higher radial conductivity deeper in the soil could yield the same results. The correlation between RLD and $d\theta(z)/dt$ is also significant ($r^2 > 0.6$), but clearly lower than between $RLD(z)$ and $U_p(z)$, because the causal relation between $d\theta(z)/dt$ and $RLD(z)$ is obscured by soil water redistribution.

Through the estimation of the "proxy" $U_p(z)$, the transpiration modulation method, combined with the SWaP sensor, can therefore also offer a simple way to estimate the relative RLD profile in soil columns close to their water-holding capacity as a first-order approximation at least for maize. In the case $U_p(z)$ equals zero, this is a good indicator of the absence of roots or at the least active roots when plant water uptake is large enough to be quantified.

However, plant-driven water-uptake profile and relative RLD do not always match. The data in Figure 5A indicates that the $U_p(z)$ peak shifts to deeper soil layers over time, while the soil column is drying out. This is not caused by inhomogeneous root growth, as otherwise Figure 5D would still show a single color, nor by passive adjustments of water uptake in response to soil water potential heterogeneity, as U_s is not included in U_p. Although for a given root system architecture $U_p(z)$ only varies with the system hydraulic properties, this phenomenon most likely results from a reduction of the hydraulic conductivity in the drier, upper half of the column between the bulk soil and root surface (Schroeder et al., 2008), at soil–root interfaces (Carminati and Vetterlein, 2013), and/or across root tissues (Hachez et al., 2012). Such reduced hydraulic conductivities would prevent both the uptake and the release of water by roots in the driest parts of the soil profile, as confirmed by isotopic experiments (Meunier et al., 2017b; Couvreur et al., 2020). Furthermore, the soil–plant hydraulic conductance would as well be reduced, which was also recently confirmed (Hayat et al., 2019), using a pressure chamber. All these studies are in line with our observation of decorrelation between $U_p(z)$ and $RLD(z)$ resulting from changing hydraulic conductivities in the soil–plant system.

Perspectives to Disentangle Soil Water Redistributive Terms, through Soil and Roots

Plant-driven RWU can be a good approximation of the actual RWU for soil columns close to water-holding capacity. However, when considerable soil water potential heterogeneities develop, passive adjustments of water uptake, $U_s(z)$, independent from $U_p(z)$ or U_{tot}, occur, leaving our estimation of RWU incomplete.

With our methodology, $U_s(z)$ is lumped with redistributive soil water flow in the $S_r(z)$ term. To disentangle these, one could estimate the soil–root system hydraulic conductance from simultaneous transpiration, soil, and stem water potential data, so that $U_s(z)$ can be estimated using the macroscopic soil–plant hydraulic model adapted by Couvreur et al. (2020), which runs in a simpler 1D domain, with few parameters. Here, using the root pressure bomb (Passioura, 1980) or the leaf pressure bomb, with which plant potential can be determined (Tyree and Hammel, 1972), might provide a solution.

The determination of $U_p(z)$ at a range of θ and θ-heterogeneity levels offers additional information compared to what is normally available, i.e. $d\theta(z)/dt$. The real RWU profile should lie in between $U_p(z)$ and $d\theta(z)/dt$, but the part of the uptake that is dependent on the shoot demand, the active part, at least can now be determined. Additional measurements and data modeling as discussed above should then allow the quantification of the true $RWU(z)$. Tracer studies can also be

used to determine $RWU(z)$, but rely heavily on modeling (Kühnhammer et al., 2020). NT clearly provides more detailed information along a limited set of roots, but heavy water must be added to the system to obtain this information, thereby changing the uptake pattern along all roots, especially in heterogeneously wetted soil. Neither of the last two methods can be applied to a large number of plants in a normal climate chamber setting, whereas the SWaP can be. The SWaP and the proposed light modulation methodology therefore offer a considerable improvement in the toolbox of plant physiologists interested in plant water usage, and should provide new insights in RWU in realistic soil environments.

MATERIALS AND METHODS

SWaP, Further Details on Hardware

The sensor part of the SWaP is a circular polyvinyl chloride (PVC) sleeve where two sheets of copper (7×5 cm^2) are glued on the inside, 9-cm apart on opposite sides (Fig. 1A). These are connected via a 2-cm–wide coil, thus forming a resonant circuit. The resonance frequency of this circuit can be determined via the so-called input reflection mode (S_{11}) of a VNA (DG8SAQ VNWA3; SDR-Kits). The VNA performs a frequency sweep (here between 150 and 220 MHz) and at the same time measures the reflected radio frequency-signals of the sensor. The minimum reflection occurs at resonance, which was extracted by a straightforward fit using a Lorentzian with a "skewed" baseline as a model, and which yields our "raw" data in the form of resonance frequencies (Fig. 1B). We linked the VNA to the sensor by means of a second single-turn coil, 2-mm apart from the coil that is part of the sensor itself, by means of inductive coupling. Inductive coupling works like a balun to the resonant circuit and, because the plates are also symmetrical, creates a symmetrical electrical field distribution throughout the object of interest. Also, cable capacitance is reduced on the sensor side, increasing dynamic range and reducing influences of parasitic capacitances, e.g. to electrical ground. The sensor was screwed into an aluminum socket (dimensions: outside diameter = 17 cm; height = 12 cm; internal diameter = 9 cm), further improving stability and noise.

The system has been multiplexed to four sensors, using a PIN diode switch (catalog no. SP4T, CDS0624; Daico Industries), with all four sensors being shifted longitudinally by a stepper motor on a linear axis (controlled via an Arduino Nano combined with an A4988 driver, programmed via the software AVR Studio 4 using the language C; https://atmega32-avr.com/). A Python script controlled the VNA and the stepper motor and performed a fit to the frequency spectra (Lorentzian and first-order polynomial) to extract the resonance frequencies of each of the four sensors at 45 vertical positions along the tubes.

SWaP, Further Details on Data Analysis

The resonance frequency, $f(z)$, of our sensor depends on the permittivity distribution relative to the E-field distribution, $E(z')$, of the sensor. We do not measure a local resonance frequency from which we would calculate a local θ, but instead we can determine the contribution, $g(z)$, of a slice of soil to the resonance frequency by repeatedly measuring the resonance frequencies at well-defined positions along the tube, e.g. in 1-cm steps in the z-direction, and perform a deconvolution afterward. For the deconvolution step, the relative local E-field strength has to be known, which we obtained by moving a 1-cm-thick, 9-cm-wide PVC disk within the sensor at 12 different z' positions (−5, −4,… 0.5, 6 cm, where 0 = middle of sensor) while measuring the resulting resonance frequency (see also further below). The local contribution to the resonance frequency at a given position can now be obtained via a deconvolution step by solving $f(z) = E(z')*g(z)$, where the asterisk denotes convolution. Ideally, a deterministic deconvolution is applied to determine $g(z)$, but noise and small deviations of $E(z')$ compared to the measured one, at the edges of the soil column, would cause distortions after deconvolution even on locations where deviations of $E(z')$ do not occur. We therefore performed a model-constrained deconvolution, by assuming that θ and therefore $g(z)$ is relatively smooth and can be approximated by a high (seventh) order polynomial, $f(z) = E(z')*[g(z) = \sum_{k=0}^{7} a_k z^k]$. When we use this to model $f(z)$, a_k values can be adjusted to minimize the squared differences with the measured resonance frequency profile. This approach requires that the resonance frequencies beyond the soil edges are known, which can easily be measured separately. Furthermore, the permittivity jumps at the soil edges should be minimized to limit perturbations of $E(z')$ at these edges. This was achieved by adding slightly wetted soil to the otherwise hollow stand for each of the four tubes and placing five water-filled 25-mL vials next to the plants on top of the soil. The described procedure then yields $g(z)$, the deconvoluted resonance frequency profile. The same procedure can also be followed to determine $dg(z)/dt$, with the advantage that the resonance frequency changes beyond the soil edges can be set to zero.

To convert $g(z)$ to $\theta(z)$, we need to calibrate our sensors. Therefore we filled fourteen 12-cm high pots (0.6 L) with oven-dried soil (loamy sand mix with two-thirds coarse sand; see van Dusschoten et al., 2016) to which known amounts of water were added to achieve the desired θ such that the average θ in the pot was between residual and saturated water content. We carefully mixed the soil shortly before measuring to achieve a homogeneous distribution of water. Each of the 14 pots was measured with the soil profiler in static mode four times. Above 16% of soil water content, gravity causes water to flow downward, which causes nonuniform water distributions. Also, upon handling, the risk of soil itself flowing downward exists. Both factors prevent the use of very wet soil being used for calibration, as resonance frequency shifts over time, and after the containers are lifted out, or lowered into, the sensors. At full saturation, soil water flows are absent, and compression can be reverted by carefully turning the closed container upside down. The values $\theta(z,t)$ and $d\theta(z,t)/dt$ can now be calculated using the calibration curve via a straightforward root-finding procedure. Summation of θ ($cm^3 \cdot cm^{-3}$) and multiplication with volume yields total amount of water of the soil column, which includes root water when a plant is present. MRI measurements of root systems can be used to correct for this error (see below).

Physical Modeling of Sensor

We simulated the complete structure of the SWaP using the platform Comsol (COMSOL Multiphysics). The simulation was used to calculate the E-field distribution of the sensor and its response to loading it with a PVC tube filled with wetted soil. Wetted soil was approximated with artificial material having a dielectric permittivity, ε_{soil} = 3, 5, 10, 15, and which was virtually placed in between the SWaP's plates. The results were then fitted to the Landau-Lifshitz/Looyenga equation (Nelson, 2005) relating θ to soil permittivity, after minor rewriting:

$$\varepsilon_{soil} = \left(\frac{\rho_{soil}}{\rho_{SiO_2}}\sqrt[3]{\varepsilon_{SiO_2}} + \Theta\cdot\sqrt[3]{\varepsilon_{H_2O}} + \left(1 - \frac{\rho_{soil}}{\rho_{SiO_2}} - \Theta\right)\right)^3, \quad (3)$$

where $4.36 < \varepsilon_{SiO_2} < 4.58$ and, $\varepsilon_{H_2O} = 81.7$ (at 150 MHz and 20°C), are the dielectric constant of quartz and water respectively, ρ_{soil} is the density of a soil (here $\rho_{soil} = 1.71\ g\cdot cm^{-3}$), and $\rho_{SiO_2} = 2.65\ g\cdot cm^{-3}$ is the (particle) density of SiO_2.

The vertical E-field distribution for the SWaP depends on the permittivity gradient within the sample. Whereas normally θ is smooth, this is not so at the edges where we expect distortions of the E-field. However, the E-field distribution needs to be sufficiently stable to perform deconvolution of the frequency data. Using Comsol, we simulated the effect of considerable jumps in permittivity. In our simulated physical model we inserted a dielectric cylinder, having dielectric constant ε_{insert}, with a diameter equal to the outer pot diameter at the bottom edge of the pot and simulated this structure when it is placed at different z-positions from the center of the SWaP. The simulated resonance frequency distributions were compared with ones based on the assumption that the E-field is unmodified by sharp changes, and the residuals were calculated as a function of ε_{insert}. For $2 < \varepsilon_{insert} < 4$, the E-field distribution had the smallest deviations from the assumed E-field distribution. Therefore we increased the E-field distribution stability at the edges of the SWaP by filling the hollow foot on which our PVC pots stand with wetted loamy soil and placing five 2.5-cm–wide vials filled with water on top of the column.

Simulations of Soil Water Flows Based on the Extended Richards Equation

To solve the extended Richards equation for our sandy soil, it is necessary to determine the soil water retention curve and obtain the van Genuchten

parameters of this soil. Furthermore, the hydraulic conductivity, $K(\theta)$ or $K(h)$, needs to be calculated for our soil using Mualem's theorem (Mualem, 1976), i.e. hydraulic conductivities $K(\theta)$ are calculated by numerical approximation of the Mualem Integral because we use a van Genuchten curve with variable parameter m (van Genuchten, 1980) implemented in Python (Bittelli et al., 2015). Here we used the same shape of $K(\theta)$ but with various K_s values (the soil conductivity for saturated soils) ranging from 2.5 to 20 cm h^{-1}.

Input $RWU(z,t)$ was modeled using a sine-function with a DC offset that prevents positive values. The resulting gradients in soil water content and potential drive the S_r. From the simulated θ-values, we computed $\hat{U}_p(z)$ in the same way we do with the experimental data.

An artificial $\hat{U}_p$ profile was constructed (a simple step function, with sum of 1) as a vector over space (45 layers) and multiplied component-wise with the total transpiration vector (entries in time direction). In this manner we obtain an imposed RWU matrix in space and time, which is then used as input for the numerical solution of the Richards equation. The 1D finite volume method is supplied with an initial $\theta(z,0)$. After this simulation of soil water content propagation, we get a discrete soil water content gradient in time and we can use the identical multiple linear regressions as discussed above to obtain $\hat{U}_p(z)$ and $S_r(z,t)$.

MRI

Three-dimensional images of the maize (*Zea mays*) roots were acquired using a 4.7-T wide bore (310 mm) magnet (Magnex) equipped with a gradient coil (internal diameter = 205 mm) with gradients up to 300 mT m^{-1}. A Varian console was used for control of the MRI experiments. Root lengths were calculated using the software NMRooting (van Dusschoten et al., 2016). Root mass density profiles were determined using a Spin Echo Multiple Slice sequence with reduced resolution ($0.75 \times 0.75 \times 4$ mm^3, compared to $0.5 \times 0.5 \times 1$ mm^3 for the normal imaging), which facilitates a shorter echo time ($TE = 4$ ms instead of 9 ms), thereby minimizing the potential artifact caused by air-filled intercellular spaces. The root mass density is required to correct θ as measured with the SWaP, because root mass cannot be discriminated from soil water based on permittivity. Especially for making correct calculations of the soil water potential, this is required. These MRI measurements were performed on regular intervals.

For a comparison of RWU profiles between 2 d, it is useful to correct for root growth, e.g. dividing $RWU(z)$ by $RLD(z)$ for the relevant days. $RLD(z)$'s values for 22 and 26 DAS (days of SWaP measurements) were interpolated values based on the MRI root images taken on 21 and 27 DAS. In this manner, maps in Figure 5C were calculated

Water Potential Measurements

For determination of the pF-curve, we used two approaches. To determine the water retention close to soil water saturation, we filled a cylinder with 45 cm of soil and wetted it from above, making sure that water was draining from the bottom. This soil column was scanned with the SWaP continuously for 8 d until no further changes in the soil water profile were detected and residual water droplets were still visible at the bottom. In that case, the water head is identical to the soil water content of these 45 cm (starting with h = 0 cm at the bottom). At the dry end of the pF-curve, we used a polymer tensiometer.

Plants and Growing Conditions

Four maize plants were grown in a climate chamber with 14- to 10-h daylight/night rhythm. Air temperature at night was set to 16°C, with 22°C during daytime. Air relative humidity at night was at 55% ± 2% and during the day at 43% ± 2%. During the day, lights were switched between 400W HPI lamps (Philips) and 400W SON-T lamps (Philips) every 2 h, resulting in a difference of light intensity between 250 and 350 and 600 to 700 μmol • m^2 s^{-1} and also 0.5°C to 1°C difference in temperature. Owing to the large temperature jump when lights are switched on the first time, the first 2 h after daybreak were not used.

Maize seeds were inserted into a soil mix (two-thirds coarse sand and one-third loamy sand from a field site near Kaldenkirchen, Germany), which was wetted close to field capacity. Seeds were left to germinate in the climate chamber. The soil was covered by a perforated piece of plastic that reduced soil water evaporation. Once the plant was longer than 4 cm, five small water-containing vials used to minimize permittivity jumps at the soil edge were placed on top of the soil. Plants were watered weekly to prevent the plants from wilting.

The soil water-content profile of each potted plant was measured every 24 min during a 3-d period and a 4-d period, each after watering, for the data analysis described here; each profile consists of 45 measurements at different depth positions ($z = 0$ at the soil surface). All profiles were independently deconvoluted, resulting in 60 profiles $g(z)$ per day. Thirty-one of these profiles, during the 12 h of light switching, were used to calculate the 45 $U_p(z)$ and $S_r(z)$ values on each of the 7 d that data were acquired for all four plants. For determination of the correlation between $RLD(z)$ and $\hat{U}_p(z)$, one plant on one of the 2 d that the soil water potential was flat (<3 kPa difference) experienced dripping water from the climate chamber ceiling so its data were rejected. Therefore, seven instances (four plants on two separate days minus one instance) could be used for the correlation. Other relevant data presented here describes results of single 12-h measurement periods of single plants (45 z-positions at 31 different time points).

Data and Code Availability

The data that support our findings of this study are available from http://www.fz-juelich.de/ibg/ibg-2/SWaP and code required to analyze the data are available at the same location.

Supplemental Data

The following supplemental materials are available.

Supplemental Figure S1. Schematic representation of relevant soil water depletion processes.

Supplemental Figure S2. E-field distribution map of a sensor.

Supplemental Figure S3. Depth profiles of $\hat{U}_p(z)$.

Supplemental Figure S4. Water head of soil water columns with growing maize plant.

Supplemental Figure S5. Simulation results from soil water depletion rates with modulated plant transpiration rates.

ACKNOWLEDGMENTS

We gratefully acknowledge Hendrik Poorter and Ralf Metzner for commenting on the article.

Received April 29, 2020; accepted August 9, 2020; published September 4, 2020.

LITERATURE CITED

Ahmed MA, Zarebanadkouki M, Kaestner A, Carminati A (2016) Measurements of water uptake of maize roots: The key function of lateral roots. Plant Soil **398:** 59–77

Ahmed MA, Zarebanadkouki M, Meunier F, Javaux M, Kaestner A, Carminati A (2018) Root type matters: Measurement of water uptake by seminal, crown, and lateral roots in maize. J Exp Bot **69:** 1199–1206

Albasha R, Mailhol J-C, Cheviron B (2015) Compensatory uptake functions in empirical macroscopic root water models: Experimental and numerical analysis. Agric Water Manage **155:** 22–39

Alm DM, Cavelier J, Nobel PS (1992) A finite-element model of radial and axial conductivities for individual roots: Development and validation for two desert succulents. Ann Bot **69:** 87–92

Baroni C, Facchi A, Gandolfi C, Ortuani B, Horeschi D, van Dam JC (2010) Uncertainty in the determination of soil hydraulic parameters and its influence on the performance of two hydrological models of different complexity. Hydrol Earth Syst Sci **14:** 251–270

Bittelli M, Campbell GS, Tomei F (2015) Soil Physics with Python: Transport in the Soil-Plant-Atmosphere System. Oxford University Press, Oxford, UK

Blum A (2009) Effective use of water (EUW) and not water-use efficiency (WUE) is the target of crop yield improvement under drought stress. Field Crops Res **112:** 119–123

Bore T, Wagner N, Lesoille SD, Taillade F, Six G, Daout F, Placko D (2016) Error analysis of clay-rock water content estimation with broadband high-frequency electromagnetic sensors—air gap effect. Sensors (Basel) **16:** 27096865

Bourzac K (2013) Water: The flow of technology. Nature **501:** S4–S6

Cai G, Vanderborght J, Couvreur V, Mboh CM, Vereecken H (2017) Parameterization of root water uptake models considering dynamic root distributions and water uptake compensation. Vadose Zone J **17:** 1–21

Caldeira CF, Jeanguenin L, Chaumont F, Tardieu F (2014) Circadian rhythms of hydraulic conductance and growth are enhanced by drought and improve plant performance. Nature Comm **5:** 5365

Caldwell MM, Richards JH (1989) Hydraulic lift: Water efflux from upper roots improves effectiveness of water uptake by deep roots. Oecologia **79:** 1–5

Carminati A, Passioura JB, Zarebanadkouki M, Ahmed MA, Ryan PR, Watt M, Delhaize E (2017) Root hairs enable high transpiration rates in drying soils. New Phytol **216:** 771–781

Carminati A, Vetterlein D (2013) Plasticity of rhizosphere hydraulic properties as a key for efficient utilization of scarce resources. Ann Bot **112:** 277–290

Chapman N, Miller AJ, Lindsey K, Whalley WR (2012) Roots, water, and nutrient acquisition: Let's get physical. Trends Plant Sci **17:** 701–710

Chaumont F, Tyerman SD (2014) Aquaporins: Highly regulated channels controlling plant water relations. Plant Physiol **164:** 1600–1618

Cooper JD (2016) Soil Water Measurement A Practical Handbook. John Wiley & Sons, West Sussex, UK

Couvreur V, Rothfuss Y, Meunier F, Bariac T, Biron P, Durand JL, Richard P, Javaux M (2020) Disentangling temporal and population variability in plant root water uptake from stable isotopic analysis: When rooting depth matters in labeling studies. Hydrol Earth Syst Sci **24:** 3057–3075

Couvreur V, Vanderborght J, Beff L, Javaux M (2014a) Horizontal soil water potential heterogeneity: Simplifying approaches for crop water dynamics models. Hydrol Earth Syst Sci **18:** 1723–1743

Couvreur V, Vanderborght J, Draye X, Javaux M (2014b) Dynamic aspects of soil water availability for isohydric plants: Focus on root hydraulic resistances. Water Resour Res **50:** 8891–8906

Couvreur V, Vanderborght J, Javaux M (2012) A simple three-dimensional macroscopic root water uptake model based on the hydraulic architecture approach. Hydrol Earth Syst Sci **16:** 2957–2971

Doussan C, Pierret A, Garrigues E, Pagès L (2006) Water uptake by plant roots: II. Modelling of water transfer in the soil root-system with explicit account of flow within the root system. Comparison with experiments. Plant Soil **283:** 99–117

Feddes RA, Hoff H, Bruen M, Dawson T, De Rosnay P, Dirmeyer P, Jackson RB, Kabat P, Kleidon A, Lilly A, et al (2001) Modeling root water uptake in hydrological and climate models. Bull Am Meteorol Soc **82:** 2797–2809

Gleason SM, Cooper M, Wiggans DR, Bliss CA, Romay MC, Gore MA, Mickelbart MV, Topp CN, Zhang H, DeJonge KC, et al (2019) Stomatal conductance, xylem transport, and root traits underpin improved performance under drought and well-watered conditions across a diverse panel of maize inbred lines. Field Crops Res **234:** 119–128

Gong Y, Cao Q, Sun Z (2003) The effects of soil bulk density, clay content and temperature on soil water content measurement using time-domain reflectometry. Hydrol Processes **17:** 3601–3614

Guderle M, Hildebrandt A (2015) Using measured soil water contents to estimate evapotranspiration and root water uptake profiles—a comparative study. Hydrol Earth Syst Sci **19:** 409–425

Hachez C, Veselov D, Ye Q, Reinhardt H, Knipfer T, Fricke W, Chaumont F (2012) Short-term control of maize cell and root water permeability through plasma membrane aquaporin isoforms. Plant Cell Environ **35:** 185–198

Halperin O, Gebremedhin A, Wallach R, Moshelion M (2017) High-throughput physiological phenotyping and screening system for the characterization of plant-environment interactions. Plant J **89:** 839–850

Hayat F, Ahmed MA, Zarebanadkouki M, Cai G, Carminati A (2019) Measurements and simulation of leaf xylem water potential and root water uptake in heterogeneous soil water contents. Adv Water Resour **124:** 96–105

Hupet F, Lambot S, Javaux M, Vanclooster M (2002) On the identification of macroscopic root water uptake parameters from soil water observations. Water Resour Res **38:** 36–31–36–14

Jarvis NJ (1989) A simple empirical model of root water uptake. J Hydrol (Amst) **107:** 57–72

Koebernick N, Huber K, Kerkhofs E, Vanderborght J, Javaux M, Vereecken H, Vetterlein D (2015) Unraveling the hydrodynamics of split root water uptake experiments using CT scanned root architectures and three-dimensional flow simulations. Front Plant Sci **6:** 370

Kühnhammer K, Kübert A, Brüggemann N, Deseano Diaz P, van Dusschoten D, Javaux M, Merz S, Vereecken H, Dubbert M, Rothfuss Y (2020) Investigating the root plasticity response of *Centaurea jacea* to soil water availability changes from isotopic analysis. New Phytol **226:** 98–110

Lobet G, Couvreur V, Meunier F, Javaux M, Draye X (2014) Plant water uptake in drying soils. Plant Physiol **164:** 1619–1627

Lynch JP, Chimungu JG, Brown KM (2014) Root anatomical phenes associated with water acquisition from drying soil: targets for crop improvement. J Exp Bot **65:** 6155–6166

McAusland L, Vialet-Chabrand S, Davey P, Baker NR, Brendel O, Lawson T (2016) Effects of kinetics of light-induced stomatal responses on photosynthesis and water-use efficiency. New Phytol **211:** 1209–1220

Meunier F, Draye X, Vanderborght J, Javaux M, Couvreur V (2017a) A hybrid analytical-numerical method for solving water flow equations in root hydraulic architectures. Appl Math Model **52:** 648–663

Meunier F, Rothfuss Y, Bariac T, Biron P, Richard P, Durand J-L, Couvreur V, Vanderborght J, Javaux M (2017b) Measuring and modeling hydraulic lift of *Lolium multiflorum* using stable water isotopes. Vadose Zone J **17:** 10.2136

Meunier F, Zarebanadkouki M, Ahmed MA, Carminati A, Couvreur V, Javaux M (2018) Hydraulic conductivity of soil-grown lupine and maize unbranched roots and maize root-shoot junctions. J Plant Physiol **227:** 31–44

Mualem Y (1976) A new model for predicting the hydraulic conductivity of unsaturated porous media. Water Resour Res **12:** 513–522

Nelson SO (2005) Density-permittivity relationships for powdered and granular materials. IEEE Trans Instrum Meas **54:** 2033–2040

Passioura JB (1980) The transport of water from soil to shoot in wheat seedlings. J Exp Bot **31:** 333–345

Rodriguez-Dominguez CM, Brodribb TJ (2020) Declining root water transport drives stomatal closure in olive under moderate water stress. New Phytol **225:** 126–134

Rothfuss Y, Javaux M (2017) Reviews and syntheses: Isotopic approaches to quantify root water uptake: a review and comparison of methods. Biogeosciences **14:** 2199–2224

Sakurai-Ishikawa J, Murai-Hatano M, Hayashi H, Ahamed A, Fukushi K, Matsumoto T, Kitagawa Y (2011) Transpiration from shoots triggers diurnal changes in root aquaporin expression. Plant Cell Environ **34:** 1150–1163

Schroeder T, Javaux M, Vanderborght J, Körfgen B, Vereecken H (2008) Effect of local soil hydraulic conductivity drop using a three-dimensional root water uptake model. Vadose Zone J **7:** 1089–1098

Sepaskhah AR, Ahmadi SH (2012) A review on partial root-zone drying irrigation. Int J Plant Prod **4:** 241–258

Simunek J, Hopmans JW (2009) Modeling compensated root water and nutrient uptake. Ecol Modell **220:** 505–521

Steudle E, Peterson CA (1998) How does water get through roots? J Exp Bot **49:** 775–788

Sydoruk VA, Fiorani F, Jahnke S, Krause H-J (2016) Design and characterization of microwave cavity resonators for noninvasive monitoring of plant water distribution. IEEE Trans Microw Theory Tech **64:** 2894–2904

Tardieu F (2012) Any trait or trait-related allele can confer drought tolerance: Just design the right drought scenario. J Exp Bot **63:** 25–31

Tyree MT, Hammel HT (1972) The measurement of the turgor pressure and the water relations of plants by the pressure-bomb technique. J Exp Bot **23:** 267–282

Vadez V, Kholova J, Medina S, Kakkera A, Anderberg H (2014) Transpiration efficiency: New insights into an old story. J Exp Bot **65:** 6141–6153

Vandoorne B, Beff L, Lutts S, Javaux M (2012) Root water uptake dynamics of *Cichorium intybus* var. *sativum* under water-limited conditions. Vadose Zone J **11:** vzj2012.0005

van Dusschoten D, Metzner R, Kochs J, Postma JA, Pflugfelder D, Bühler J, Schurr U, Jahnke S (2016) Quantitative 3D analysis of plant roots growing in soil using magnetic resonance imaging. Plant Physiol **170:** 1176–1188

van Genuchten MT (1980) A closed-form equation for predicting the hydraulic conductivity of unsaturated soils. Soil Sci Soc Am J **44:** 892–898

Wasson AP, Richards RA, Chatrath R, Misra SC, Prasad SVS, Rebetzke GJ, Kirkegaard JA, Christopher J, Watt M (2012) Traits and selection strategies to improve root systems and water uptake in water-limited wheat crops. J Exp Bot **63:** 3485–3498

York LM, Carminati A, Mooney SJ, Ritz K, Bennett MJ (2016) The holistic rhizosphere: Integrating zones, processes, and semantics in the soil influenced by roots. J Exp Bot **67:** 3629–3643

Zarebanadkouki M, Kim YX, Carminati A (2013) Where do roots take up water? Neutron radiography of water flow into the roots of transpiring plants growing in soil. New Phytol **199:** 1034–1044

Zarebanadkouki M, Meunier F, Couvreur V, Cesar J, Javaux M, Carminati A (2016) Estimation of the hydraulic conductivities of lupine roots by inverse modelling of high-resolution measurements of root water uptake. Ann Bot **118:** 853–864

Zimmermann U, Münnich KO, Roether W, Kreutz W, Schubach K, Siegel O (1966) Tracers determine movement of soil moisture and evapotranspiration. Science **152:** 346–347